ISPRS Journal of Photogrammetry and Remote Sensing 189 (2022) 128–142

Contents lists available at ScienceDirect

ISPRS Journal of Photogrammetry and Remote Sensing

journal homepage: www.elsevier.com/locate/isprsjprs

Improvements in GPR-SAR imaging focusing and detection capabilities of UAV-mounted GPR systems

María García-Fernández, Guillermo Álvarez-Narciandi, Yuri Álvarez López *, Fernando Las-Heras Andrés

Área de Teoría de la Señal y Comunicaciones, Universidad de Oviedo, Campus Universitario de Gijón, 33203 Gijón (Asturias), Spain

ARTICLE INFO

Keywords:
Ground penetrating radar
Synthetic aperture radar
Unmanned aerial vehicle
Singular value decomposition
Landmines
Improvised explosive devices
Co-registration

ABSTRACT

In recent years there has been an increasing research interest in the development of airborne-based Ground Penetrating Radar (GPR) systems for safe and fast detection of buried threats such as landmines and Improvised Explosive Devices (IEDs). Compared to other sensors such as metal detectors or magnetometers, GPR is able to detect either metallic and non-metallic targets. Besides, the use of Ultra Wide Band (UWB) radiofrequency hardware allows retrieving high resolution images of the subsoil, thus improving the detection capabilities. Airborne-based GPR systems are affected by uncertainties that need to be characterized and corrected. This contribution focuses on the following three issues: (i) influence of the height information in the GPR-Synthetic Aperture Radar (GPR-SAR) images, determining which sensors provide better quality images; (ii) distortion of the imaged targets in along-track axis due to small tilting of the UWB antennas on board the UAV, proposing a co-registration technique to correct it; and (iii) revision of SVD filtering techniques, assessing a criterion to classify the different eigenimages. The analysis of these issues, as well as the validation of the proposed correction methods, are conducted using measurements taken during validation campaigns of the implemented airborne-based GPR system. For this purpose, two validation scenarios with different soil characteristics have been selected. Metallic and non-metallic targets with different shapes and sizes have been buried in them. In the case of the first scenario (wet loamy soil), detection capabilities improved from 50% (5 out of 10 targets were detected) to 80%. For the second validation scenario (loamy soil, but less humid than the first scenario), not only a 100% detection is achieved, but also the targets are clearly imaged in the GPR-SAR images obtained with the improvements presented in this contribution.

1. Introduction

1.1. Context and background

Ground Penetrating Radar (GPR) has become a key technology for Non-Destructive Testing (NDT), which encompasses a wide scope of applications, such as infrastructure inspection (Lee et al., 2004) or detection of across-border tunnels (Martinez-Lorenzo et al., 2011). The operation principle of GPR is the reflection of electromagnetic waves created by changes in the constitutive parameters (conductivity, σ, and permittivity, ε) of materials (Leuschen and Plumb, 2001; Jol, 2009).

In the field of landmine and Improvised Explosive Devices (IEDs) detection, GPR has several advantages over other well-established technologies (e.g., metal detectors (Sato et al., 2005; Minekafon project, 2021), electromagnetic induction (Won et al., 2001), and magnetometers (Yoo et al., 2020)). These technologies are mainly limited to metallic targets, whereas GPR is able to detect both metallic and non-metallic threats (Daniels, 2006; Peichl et al., 2014; Bestagini et al., 2021). Hyperspectral imaging has become a promising technology for the detection of shallow landmines, as described in Makki et al. (2017), proposing the combination of GPR and hyperspectral sensors to overcome the limitations in terms of penetration depth of the latter. Concerning the GPR capability to detect buried targets, the working frequency band has to be chosen as a trade-off between the desired resolution of the system (the larger the bandwidth, the better the down-range resolution) and the penetration depth (signal attenuation increases with frequency).

With regard to landmine and IED detection systems, handheld detectors have been widely employed (e.g. a GPR and a metal detector integrated in a handheld system is presented in Sato et al. (2005)).

* Corresponding author.
E-mail address: alvarezyuri@uniovi.es (Y. Álvarez López).

https://doi.org/10.1016/j.isprsjprs.2022.04.014
Received 10 November 2021; Received in revised form 19 April 2022; Accepted 19 April 2022
Available online 14 May 2022

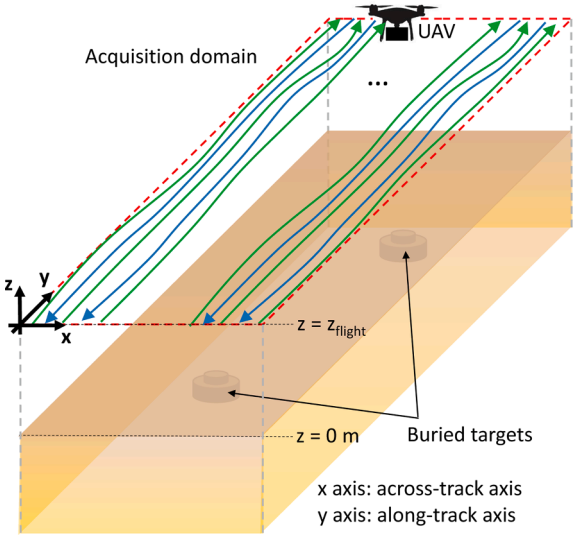

Fig. 1. Illustration of the flight path followed by the airborne-based GPR system. Orientation of the along-track sweeps towards +y and towards -y is denoted with green and blue arrows, respectively.

However, although direct contact between the detector and the ground is avoided with handheld detectors, there is a risk for the human operator in case of a missed target. Remotely-controlled scanning systems, as the autonomous robots presented in Gonzalez et al. (2005), Ismail et al. (2014), provide a higher safety level, but at the expense of reduced scanning throughput since they move slowly over the inspected area.

In general, any ground system for IED and landmine detection has an inherent risk of accidental detonation. Consequently, there has been an increasing interest in the development of airborne-based landmine and IED detection systems leveraging the advances in Unmanned Aerial Vehicles (UAVs) technology. In recent years, small, lightweight radar modules have been successfully integrated on board UAVs for Synthetic Aperture Radar (SAR) imaging as described in Hügler et al. (2018), Noviello et al. (2021), and in Section 5.3 of Colomina and Molina (2014), enabling the detection of small ground features such as tripwires (Klein et al., 2020).

Different architectures of airborne-based landmine and IED detection systems have been proposed. For example, Down-Looking GPR (DL-GPR) architectures have been considered in Colorado et al. (2017), Sipos and Gleich (2020), Noviello et al. (2021), Schreiber et al. (2019), Roussi et al. (2019) and Garcia-Fernandez et al. (2020), whereas an airborne side-looking GPR is presented in Schartel et al. (2020, 2021). Furthermore, centimeter-level geo-referring and positioning capabilities have enabled the introduction of SAR processing in airborne-based GPR systems (e.g. in Schartel et al. (2020), Garcia-Fernandez et al. (2020)), resulting in enhanced detection capabilities. Moreover, improvements in computing capabilities have made possible the GPR-SAR processing of large amounts of measurements, thus avoiding the need of subsampling or sparse schemes (Noviello et al., 2021) that degrade the detection capabilities (which is especially critical in the field of landmine and IED detection). In Table 1 of Garcia-Fernandez et al. (2020) a summary of the specifications of the aforementioned airborne-based GPR systems can be found. It can be noticed that the majority operate in the L and S bands (1–4 GHz), as this frequency range offers a good trade-off between penetration depth and image resolution (free-space down-range resolution is around 5–7 cm).

Besides the intrinsic challenges associated to GPR-SAR processing, airborne-based systems introduce additional uncertainties that have to be properly addressed to produce high-resolution GPR images of the underground. For example, radar measurements are not uniformly distributed due to the deviation of the platform where the GPR is embedded from the ideal flight path. These deviations are inherent to UAVs and are caused by several factors (e.g. wind gusts). In this sense, a scanning strategy to avoid across-track aliasing must be implemented (e.g., a two-dimensional (2D) scanning strategy where consecutive along-track sweeps are spaced a few centimeters).

Similarly to ground-based GPR systems, air-launched GPR architectures can be divided in two main groups: Forward-Looking GPR (FL-GPR) and DL-GPR. The former architecture captures less clutter from the air-ground reflection (Comite et al., 2018; Comite et al., 2021), whereas the latter exhibits a higher dynamic range (Rosen and Ayers, 2005). Thus, in the case of DL-GPR, one of the main challenges is the detection of shallow targets as they can be masked by the air-ground reflection (van der Merwe and Gupta, 2000).

1.2. Aim and scope

This contribution addresses several challenges related to UAV-based GPR systems: the accurate determination of the height above ground of the UAV, the improvement in the focusing of the GPR-SAR images, and the mitigation of the clutter. In particular, the following techniques have been proposed to improve the performance of the UAV-based GPR system:

- A method to estimate the height above ground from GPR measurements has been presented and validated. Results show that the height estimations obtained with this technique enable the retrieval of higher quality GPR-SAR images with respect to the height information provided by other sensors commonly used in UAV-based GPR systems.
- A co-registration procedure to compensate the different antenna tilt and, therefore, the different radar look angle in forward and backward sweeps, yielding GPR-SAR images better focused and with less clutter.
- A new SVD filtering technique capable of automatically discarding the eigenimages which mainly contain clutter coming from the strong reflections on the air-ground interface. These eigenimages are removed before the GPR-SAR processing is conducted. As a result, the clutter of the retrieved GPR-SAR images is reduced and the detection capabilities of the system are significantly improved.

Measurements taken with the airborne-based GPR system described in Garcia-Fernandez et al. (2020) will be used to illustrate the aforementioned issues as well as to validate the techniques proposed in this contribution.

2. Materials and methods

The airborne-based DL-GPR system used in this contribution is based on a commercial airframe (Spreading wings, 2021) with 11 kg maximum take-off weight. Several off-the-shelf sensors and systems have been integrated in this platform to enable GPR measurements geo-referred with centimeter-level accuracy. The GPR subsystem consists of an Ultra Wide Band (UWB) radar module (m:explore, 2021) whose frequency band ranges from 100 MHz to 6 GHz. It also has two receiving ports, so three UWB antennas can be mounted on board the UAV following a receiving-transmitting-receiving arrangement as shown in Garcia-Fernandez et al. (2020).

The selected UWB antennas operate from 600 MHz up to 6 GHz (TSA600, 2021). They were chosen as a trade-off between size and working frequency band. In particular, they are less bulky than the customized design presented in Schartel et al. (2020), Sipos and Gleich (2020), allowing an easier integration within the UAV frame.

The flight operation mode is summarized next: a flight path is defined over the area to be scanned using waypoints, so that the UAV will follow these waypoints after taking-off. Along-track sweeps are alternatively performed in the forward and backward direction with respect to the UAV heading, thus avoiding 180° turns at the end of each

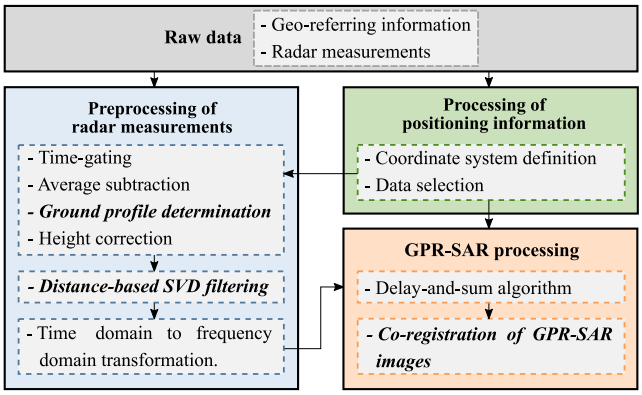

Fig. 2. Scheme illustrating the processing workflow of the geo-referred radar measurements. Steps highlighted in bold correspond to the improvements presented in this contribution.

sweep. These turns would worsen the UAV flight performance and increase the flight time, consequently reducing the effective time the UAV is performing the scan over the area of interest. Fig. 1 illustrates the flight operation mode. The methodology to compute the reflectivity images conducting the SAR processing is based on that presented in Garcia-Fernandez et al. (2020), Gonzalez-Diaz et al. (2020), Garcia-Fernandez et al. (2019), which has been modified to include the techniques presented in this manuscript. The workflow of this methodology, which uses a delay-and-sum algorithm (Johansson and Mast, 1994), is summarized in Fig. 2, where the additional processing steps proposed in this contribution are highlighted in bold.

3. Theory

3.1. Determination of the ground profile

A key issue to obtain high-resolution GPR-SAR images is the accurate geo-referring of GPR measurements. To achieve this, the system presented in Garcia-Fernandez et al. (2020) uses mainly a Global Navigation Satellite System - Real Time Kinematics (GNSS-RTK) receiver (GNSS-RTK, 2020) together with a laser rangefinder (LIDAR, 2020), having these sensors a vertical accuracy of 1 cm and 1.8 cm, respectively. The positioning information provided by these sensors is complemented with the one obtained from standard positioning sensors found in UAV systems (compass, inertial measurement unit, conventional GNSS receiver, barometer).

In the case of air-launched GPR systems, accurate measurement of the height above ground is required for a proper identification of the air-soil interface. As studied in Clark et al. (2005, 2006), soil roughness has an impact in the detection capabilities of GPR systems, especially concerning the detection of shallow targets. Furthermore, GPR-SAR-based techniques are more sensitive to uncertainties in height determination as GPR measurements need to be processed coherently.

UAV height information is directly obtained from the laser rangefinder and the GNSS-RTK sensors. Besides, this contribution proposes a technique to recover the ground profile from the radar measurements of the GPR on board the UAV. A comparison between height information obtained using a laser rangefinder, GNSS-RTK, and a 1-GHz bandwidth radar has been conducted in Schartel et al. (2018). It must be pointed out that, in this case, the higher frequency band of the radar (26 GHz) limits its use for GPR applications. The use of interferometric SAR to retrieve the ground profile has been proposed in Burr et al. (2021), where the 6–9 GHz frequency band is selected for ground profile mapping while keeping the 1–4 GHz frequency band for GPR. In Ludeno et al. (2018) the air-soil interface is detected by applying an edge detection technique to the radar measurements, which were taken in the 3.1–4.8 GHz frequency band.

In this contribution, the time-domain signal provided by the UWB radar is used to estimate the height of the UAV. First, a spatial filter and an average subtraction technique are applied to the radar signals to remove unwanted contributions (mainly the TX-RX couplings). Then, for each radar measurement, the partial energy curve is calculated as explained in S.M.M. et al. (2008). In particular, for each radar measurement, the s-th sample of the partial energy curve is defined as follows:

$$S_s = \sum_{p=1}^{s} \left(x_p^2 - s\delta \right), \tag{1}$$

where $s \in [1, N_S]$, x_p if the p-th sample of the radar measurement, and δ, which is given by

$$\delta = S_T / N_S, \tag{2}$$

is a trend that depends on the total energy of the radar measurement, S_T, and its number of samples, N_S. The global minimum of this curve is located at the arrival time of the radar signal, which in turn corresponds to the air-soil interface. There is a small systematic offset between the arrival of the signal and the position of the interface, which depends on the radar waveform (for this radar, it is corrected by summing 6 cm to the estimated arrival position). It must be noted that this technique is more robust than just selecting the maximum of the radar signal, which can be affected by factors such as noise. The procedure to estimate the height for one radar measurement is depicted in Fig. 3.

The height above ground obtained from several radar measurements is compared with the laser rangefinder and GNSS-RTK information in Fig. 4. It can be observed that RTK height information cannot be used to estimate the distance from the UAV to the ground, especially in the case of large scenarios. The reason is that RTK height information uses a reference geoid that does not represent local variations of the terrain (i.e., RTK height corresponds to the height over the geoid, not over the terrain). The height information provided by the laser rangefinder and estimated from the radar measurements exhibit a similar behavior. The impact of the height extracted from the laser rangefinder and the radar measurements on GPR-SAR processing will be analyzed in Section 4.

3.2. Spatial alignment in along-track direction

As previously discussed, the scanning strategy to inspect a given area avoiding across-track aliasing consists of performing consecutive along-track sweeps separated a few centimeters (5 cm in this case), as depicted in Fig. 1. Due to the different throttle applied to the UAV propellers by

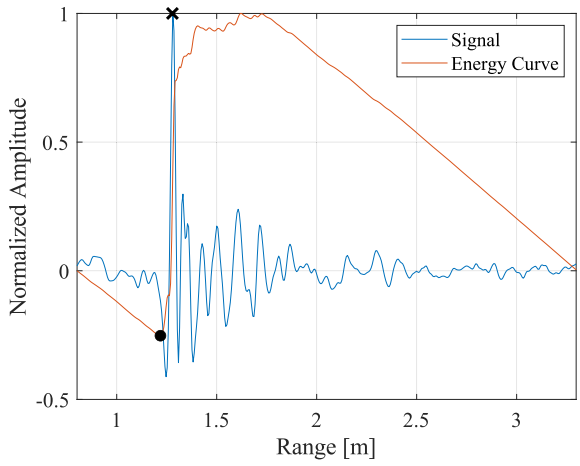

Fig. 3. Estimation of the height information using the GPR radar module for one measurement: radar signal (blue), partial energy curve (orange), arrival of the signal (black dot) and estimated height (black x-mark).

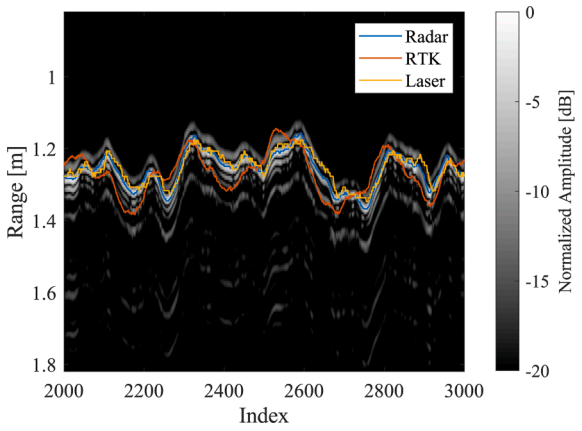

Fig. 4. Comparison of the height information provided by the GPR radar module (blue), the GNSS-RTK (orange), and the laser rangefinder (yellow). Background: intensity of the radar signal for the first RX channel after average subtraction.

the flight controller during forward (+y) and backward (−y) sweeps, the UWB GPR antennas have a slightly different tilt with respect to the ground, i.e., the radar look angle is slightly different in the forward and backward sweeps. As a result, the GPR-SAR image is not perfectly focused when considering both forward and backward sweeps. An analogous issue arises in the context of satellite-based SAR imaging (Gauthier et al., 1998; Plotnick and Marston, 2018) (e.g., when the same area is inspected at different times and/or from different viewpoints).

The effect of this problematic can be observed in Fig. 5. In this case, two metallic flat and symmetric targets were buried 13 cm deep (Fig. 5 (a)) and a scan of an area of 2 m × 4 m was performed with the airborne-based GPR system. In Fig. 5 the GPR-SAR images of the calibration

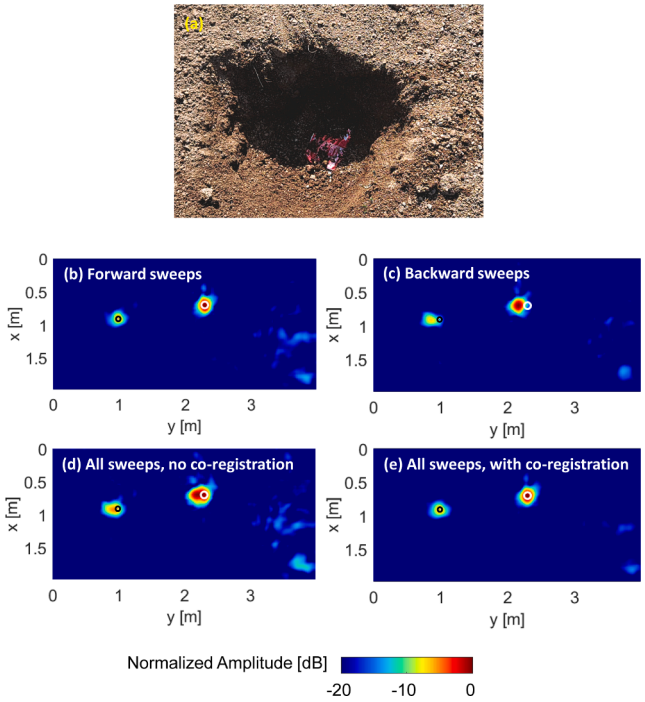

Fig. 5. Example of SAR images distortion due to along-track offset: buried metallic target (flattened red can) for system calibration (a) and GPR-SAR images (cut z = −13 cm) from forward sweeps (b), from backward sweeps (c), from all sweeps before applying co-registration correction (d), and from all sweeps after applying co-registration correction (e). Black and white circumferences are centered at the position where the targets are detected in (e).

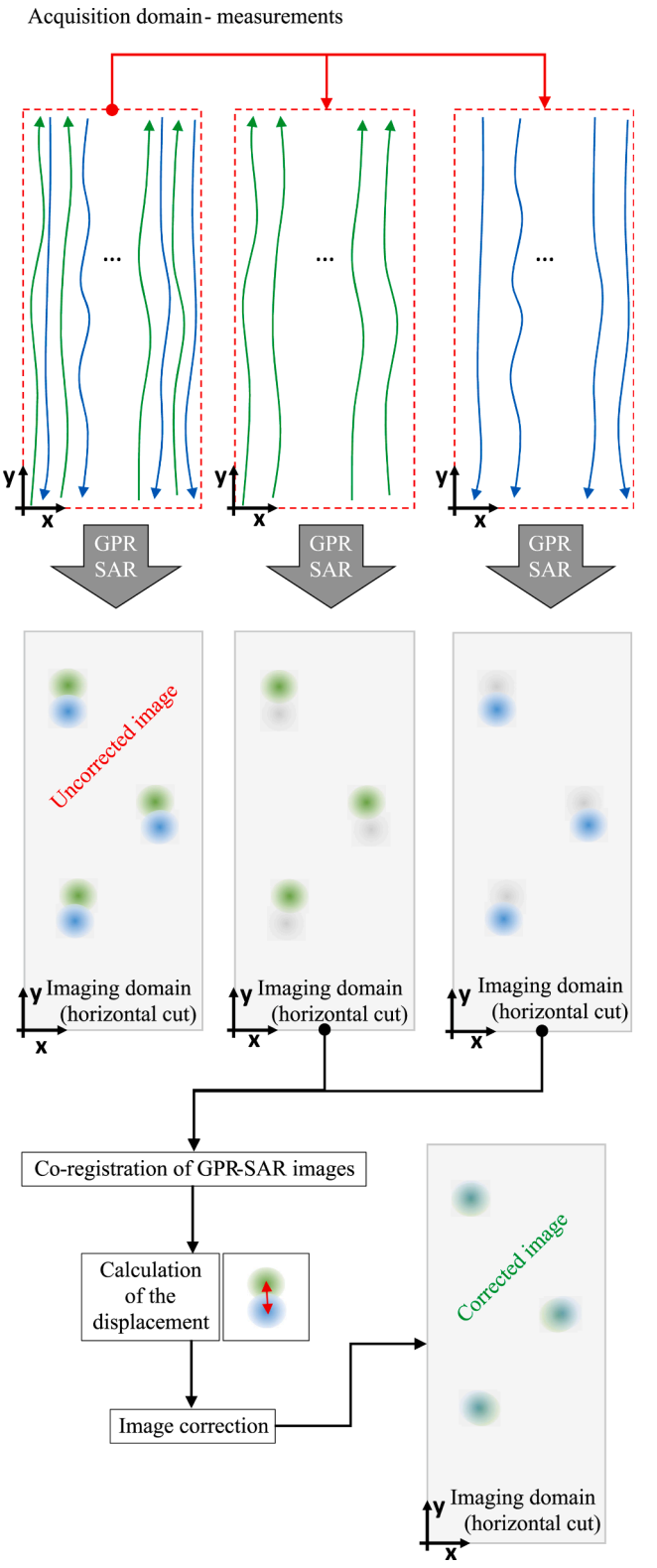

Fig. 6. Scheme illustrating the co-registration technique. Green color: +y axis along-track sweeps and targets imaged when these sweeps are considered. Blue color: -y axis along-track sweeps and targets imaged when these sweeps are considered.

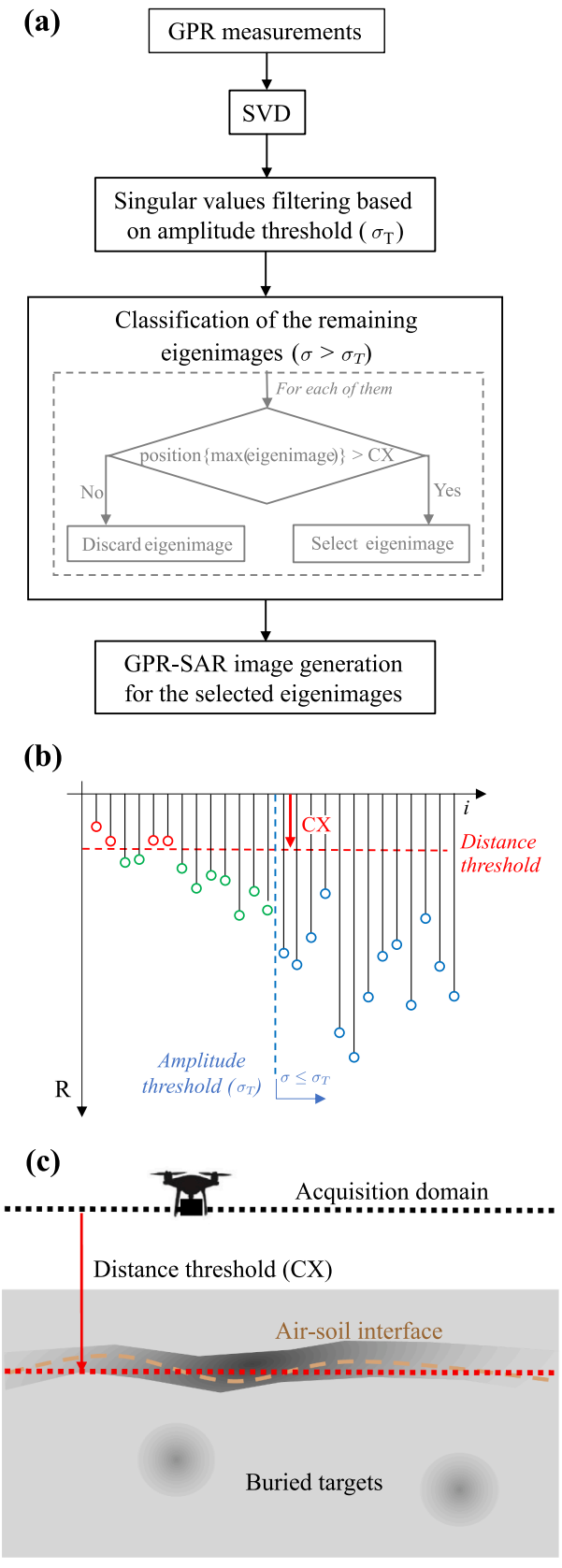

Fig. 7. Scheme illustrating the SVD filtering technique presented in this contribution. (a) Flowchart. (b) Singular values filtering based on the range (R) of the maximum of the eigenimages, and the level (σ) of each of the singular values. Remaining singular values are depicted in green and the filtered ones are shown in red (those below CX) and blue (those below the amplitude threshold). (c) Definition of the distance threshold (CX).

targets are compared when considering forward sweeps only, Fig. 5 (b), backward sweeps only, Fig. 5 (c), and all sweeps without a correction technique, Fig. 5 (d). As it can be seen, the position of the target in the SAR images obtained considering forward and backward sweeps independently is shifted. In addition, when measurements from all sweeps are processed the image of the target is distorted, i.e., it appears elongated in along-track direction. At this point it should be noted that the UAV flight height is usually set around 1.5 m above the ground, so a tilting as small as 1.15° with respect to the z (vertical) axis would result in a 3 cm displacement on the ground (i.e., a 6 cm offset when combining +y and −y sweeps).

To correct this offset, a co-registration technique has been implemented. This technique consists of obtaining two independent GPR-SAR images, one corresponding to the sweeps towards +y (green arrows in Fig. 1 and Fig. 6) and the other corresponding to the sweeps towards −y (blue arrows in Fig. 1 and Fig. 6). Then, these images are registered based on their intensity. For this purpose, the image corresponding to the sweeps towards +y, f_{fw}, is chosen as a reference, whilst the image corresponding to the backward sweeps, f_{bw}, is transformed to match the former. This transformation, $\widehat{T}$, aims to maximize the similarity between the intensity of the images to be registered (which is measured with a metric called Mattes Mutual Information, MMI, (Mattes et al., 2001)). In particular, $\widehat{T}$, is obtained minimizing the negative of MMI as follows:

$$\widehat{T} = \arg\min_{T} -\mathrm{MMI}\left(f_{fw}, T\{f_{bw}\}\right). \tag{3}$$

The minimization problem is solved employing an iterative non-linear optimization algorithm called (1 + 1)-Evolution Strategy, which has been successfully employed for registering Magnetic Resonance images (Styner et al., 2000). Finally, once the transformation has been found the reference image, f_{fw}, and the transformed image, $\widehat{T}\{f_{bw}\}$, are coherently combined, i.e., taking into account the amplitude and phase. It should be remarked that only the intensity is considered to find the transformation, and there is no need to use fiducial targets. The scheme of the presented co-registration procedure is illustrated in Fig. 6, and the GPR SAR image of the calibration targets depicted in Fig. 5 (a) obtained after applying the co-registration technique is shown in Fig. 5 (e). As it can be observed, in contrast to Fig. 5 (d) (without co-registration), not only the shape of the targets is better reconstructed (it is sharper and symmetric), but also the clutter is reduced.

3.3. SVD-based clutter removal techniques

A key issue to achieve accurate detection of buried targets is to maximize the signal-to-clutter ratio in the recovered GPR-SAR images. This is of special relevance in GPR (Solimene et al., 2014), where different techniques have been proposed depending on the architecture and features of the GPR system. For example, (van der Merwe and Gupta, 2000) introduces the use of basis functions for clutter representation, proving their success for the detection of large targets. Other authors (e.g. (Lopera et al., 2007)) propose a more complete model of the system including the air-ground reflection and the interaction between the antenna and the ground. The simulated fields, intended to model clutter as accurate as possible, are subtracted from GPR measurements.

Other techniques for clutter mitigation in GPR systems are based on Singular Value Decomposition (SVD) filtering (Abujarad et al., 2018; Garcia-Fernandez et al., 2017; Bi et al., 2018). In particular, in Abujarad et al. (2018) the authors propose two methods based on SVD filtering after average subtraction. The first one is based on removing the eigenimages corresponding to the k-th last singular values, which are identified as clutter, and the second one is based on computing an estimation of the background and the target from the eigenimages (in particular, they just consider the second largest singular value as the background and the rest as part of the target). In Bi et al. (2018) a SVD filtering

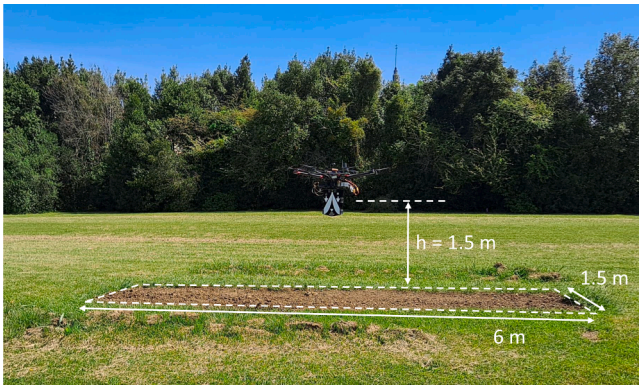

Fig. 8. Picture of the UAV prototype while scanning the first validation scenario.

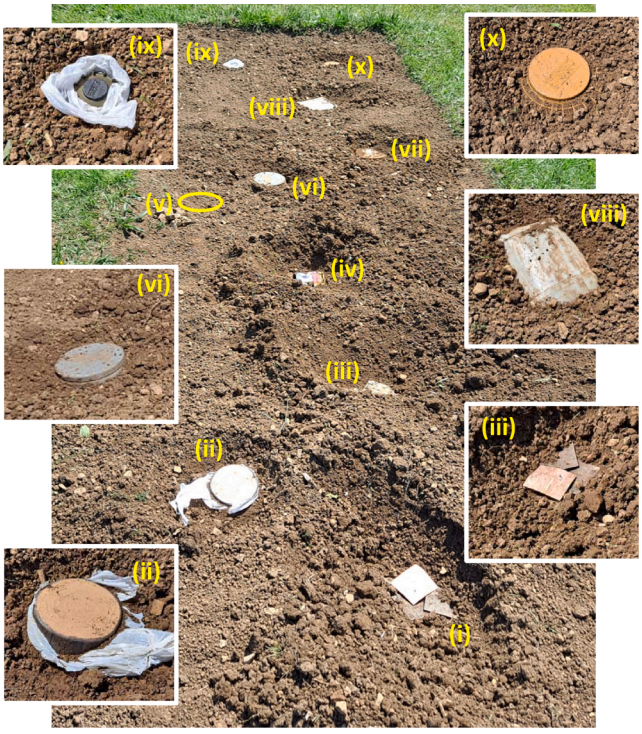

Fig. 9. Picture of the targets buried in the first validation scenario.

method based on the Hankel Matrix was proposed. Analogously, in Garcia-Fernandez et al. (2017) an SVD filtering procedure is applied to the reflectivity image obtained after the GPR processing.

In contrast to previous approaches, in this paper a novel SVD filtering technique, which is applied to the raw radar measurements after average subtraction and height correction, is presented. The proposed technique focuses on mitigating the clutter produced by the strong reflections on the air-ground interface. In contrast to Garcia-Fernandez et al. (2020) (where just the first eigenimage was removed as it usually contains air-ground interface contributions), the presented method enables to automatically classify the singular values that belong to the clutter, which can be removed before the GPR processing, based on the range of the maximum of their corresponding eigenimages.

Each radar data matrix, Y, has N_M radar measurements of N_S samples each. After applying SVD, the $N_M \times N_S$ matrix can be decomposed into $N_I = min(N_M, N_S)$ eigenimages as

$$Y = USV^H = \sum_{i=1}^{N_I} u_i \sigma_i v_i^H, \tag{4}$$

where S is the diagonal matrix that contains the singular values, σ_i, of the data matrix in descending order, i.e., $\sigma_1 \geqslant \sigma_2 \geqslant \ldots \geqslant \sigma_{N_I}$. U and V are the unitary matrices that contain the singular vectors, u_i and v_i, respectively, and H denotes the Hermitian transpose. After decomposing the data matrix into the N_I eigenimages, the filtering is performed according to the scheme depicted in Fig. 7 (a). First, the eigenimages associated to the singular values below a certain threshold (σ_T) are removed, as they are likely to represent noise present in the measurements (in particular, $\sigma_T = 0.01\sigma_1$, where σ_1 is the highest singular value). Then, the remaining eigenimages are classified analyzing the position (i.e., range) of their maximum. As shown in Fig. 7, the proposed criterion is based on removing those eigenimages whose maximum is located closer to the radar than a certain distance (hereinafter denoted as CX, where X is the distance in cm). This distance corresponds approximately to the location of the air-ground interface (see Fig. 7 (c)). The idea behind this criterion is that if the maximum of the eigenimage is found below this distance it is likely to correspond to the air-ground reflection, whereas if the peak is found further (i.e. deeper in the ground), it could correspond to a buried target. The filtered data matrix, $\widehat{Y}$, can be expressed as

$$\begin{aligned} \widehat{Y} &= \sum_{k \in \{1,\ldots,N_I\}} u_k \sigma_k v_k^H, \\ &\text{subject to} \quad \begin{array}{l} \text{position}\left\{\max\left(u_k \sigma_k v_k^H\right)\right\} \rangle \mathrm{X}\ [\mathrm{cm}], \\ \sigma_k > \sigma_T \end{array} \end{aligned} \tag{5}$$

which is then further processed applying the masked SAR processing proposed in Garcia-Fernandez et al. (2020) to retrieve the resulting GPR-SAR image.

The value of the distance threshold CX is derived from the average value of the height above ground estimated from radar measurements as detailed in Section 3.1, $h_{soil-radar}$. It should be noted that, as outlined in Fig. 2, the SVD filtering is performed after the height correction step introduced in Garcia-Fernandez et al. (2019) to account for potential terrain irregularities. Based on the experience gathered during extensive experimental campaigns, the threshold is set in the range $h_{soil-radar} + [0.75 - 1.25]\lambda_0^{min}$, where λ_0^{min} is the wavelength in free-space at the

Table 1
Buried targets in the first validation scenario.

Object	Size (cm)	Depth (cm)	Other specs.
(i) First group of metallic plates	10 × 10 (5 × 5 each)	14	3 plates
(ii) Wooden trunk-like IED	25 long × 15ø Vert. placed	1	No metal content
(iii) Second group of metallic plates	10 × 10 (5 × 5 each)	14	3 plates
(iv) Metallic can (cylindrical)	12ø × 14 long	18	Can lids perpendicular to air-ground interface
(v) Third group of metallic plates	10 × 10 (5 × 5 each)	8	3 plates
(vi) Two stacked plastic disks	18ø × 2 thick	2	
(vii) Metallic disk	18ø	9	
(viii) 7.5 litre plastic jug (empty)	29 long × 22 wide × 12 thick	1	
(ix) TS-50 anti-personnel landmine(TS-50, 2021)	9ø × 4.5 thick	1	Minimum metal content
(x) VS-1.6 anti-tank landmine (VS-1.6, 2021)	22ø × 9.2 thick	5	No metal content

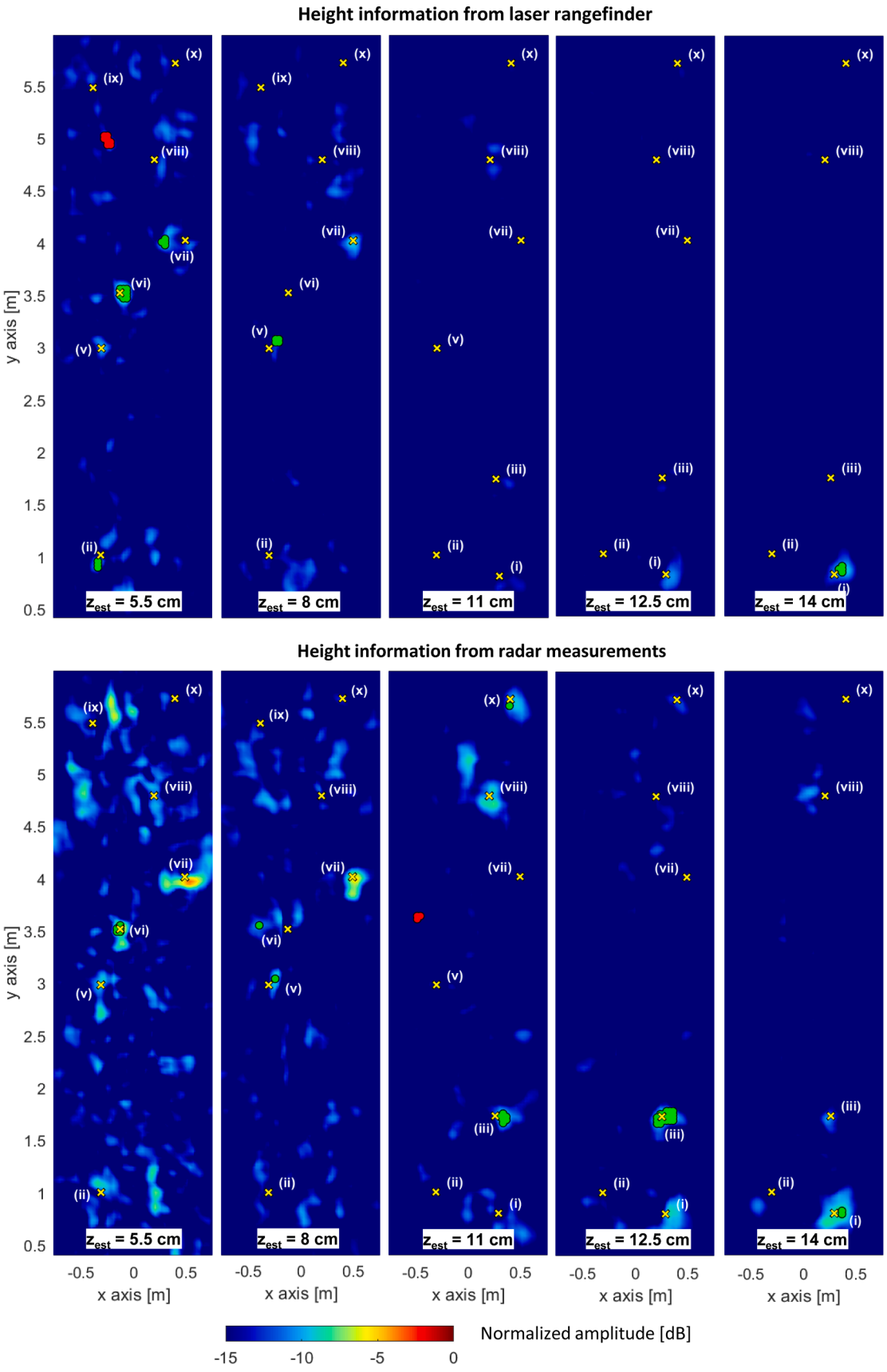

Fig. 10. Detection results in the first validation scenario when using height information from the laser rangefinder (upper row) and from the radar measurements (lower row). SVD filtering applied: three first singular values are removed.

Table 2
Targets found by the CFAR detector in the GPR-SAR images shown in Fig. 10 and Fig. 11.

Object	Laser, SVD S3	Radar, SVD S3	Laser, SVD C137.5	Radar, SVD C137.5
(i) First group of metallic plates	14 cm	14 cm	12.5 cm	14 cm
(ii) Wooden trunk-like IED	5.5 cm		11 cm	
(iii) Second group of metallic plates		11 cm, 12.5 cm	11 cm, 12.5 cm	11 cm, 12.5 cm
(iv) Metallic can (cylindrical)				
(v) Third group of metallic plates	8 cm	8 cm	5.5 cm, 8 cm	5.5 cm, 8 cm, 11 cm
(vi) Two stacked plastic disks	5.5 cm	5.5 cm, 8 cm	5.5 cm	5.5 cm
(vii) Metallic disk	5.5 cm			8 cm
(viii) 7.5 litre plastic jug (empty)				11 cm
(ix) TS-50 anti-personnel landmine(TS-50, 2021)				
(x) VS-1.6 anti-tank landmine (VS-1.6, 2021)		11 cm		11 cm

maximum operational frequency.

4. Results

Measurements collected in two validation campaigns of the airborne-based GPR system will be used to illustrate the issues described in Section 3 as well as to validate the proposed correction techniques.

4.1. First validation scenario

The first validation scenario is a 6 m length × 1.5 m width area within the airfield of the University of Oviedo (Gijón, Spain), shown in Fig. 8 and Fig. 9.

An estimation of the constitutive parameters of the soil is required to calculate the propagation wavespeed of electromagnetic waves when propagating in the ground, resulting in a correct estimation of the depth of the targets. Different methods to obtain the permittivity and moisture of the soil have been developed, ranging from theoretical models to *in-situ* measurements (Neusch and Sties, 1999; Lambot et al., 2004; Llossera et al., 2005; Hasan et al., 2014). In this contribution, the relative permittivity (ε_r) of the soil was estimated from GPR-SAR measurements following the methodology described in Alvarez et al. (2017), which makes use of a reference target whose depth is known. For the first validation scenario, the relative permittivity was found to be within $\varepsilon_r = 6$ to $\varepsilon_r = 7$, in agreement with the value of the relative permittivity for this kind of soil and moisture level (Lambot et al., 2004; Llossera et al., 2005).

GPR-SAR measurements were conducted at a height of 1.5 m above the ground, as it provides a good trade-off between flight stability (minimization of ground effect) and free-space attenuation of the incident and reflected radar signals. The surveyed area of 6 m × 1.5 m was discretized into 31 along-track sweeps, being 75 cm/s the flight speed. Spacing between sweeps was 5 cm, that is $\lambda/2$ at the highest frequency of the considered frequency band for GPR-SAR processing (from 600 MHz to 3 GHz). A picture of the UAV scanning the scenario is shown in Fig. 8 and a video of the UAV can be watched in the provided multimedia file entitled “videoExample1.mp4”.

Different kinds of targets were buried, either metallic and non-metallic, with different geometries and depths. These targets are described in Table 1 and a picture of them in the airfield can be found in Fig. 9.

For a further comparison of the detection results achieved with the different techniques introduced in this contribution, reflectivity images were processed using a Constant False Alarm Rate (CFAR) detector. More precisely, the CFAR detector is a standard version of the cell-averaging CFAR detector (CA-CFAR) (Taylorl, 2019), which estimates the noise variance for the cell under test within the GPR-SAR image by selecting a range of neighboring cells. The CA-CFAR detector assumes that the noise in the neighboring cells follows the same distribution as in the cell under test, and that there are no targets in these neighboring cells. To improve the performance of the CA-CFAR detector, buffer or guard cells have to be kept between the cell under test and the neighboring cells. The main parameters to be adjusted in the CA-CFAR detector are the probability of false alarm, the number of neighboring cells, and the number of guard cells. These parameters have been adjusted following a trial-and-error procedure using a dataset of GPR-SAR images.

In the GPR-SAR images presented in this section, CFAR detection results are highlighted in green and red colors. Pixels highlighted in green color are located less than 30 cm away from the true position of the target, so it can be considered a correct detection, whereas the red ones correspond to false alarms.

The depth (z axis) of the GPR-SAR images depicted in this contribution is corrected taking into account the estimated relative permittivity of the soil. For the first scenario, a relative permittivity $\varepsilon_r = 6.5$ is considered.

The GPR-SAR images and the detection results when using laser rangefinder or radar height information are analyzed in Fig. 10 - Fig. 14 and in Table 2. As it can be observed, the best detection results are achieved when radar height is used. For example, in Fig. 10, where the same SVD filtering is applied, the second group of metallic plates (iii) and the VS-1.6 anti-tank landmine (x), are only detected when radar height is used (Fig. 10, bottom row). Also, the 7.5 litre plastic jug (viii) is better imaged when considering radar height.

The improvement is noticeable in vertical cuts of the GPR-SAR images. Fig. 12 corresponds to the XZ cut centered at the position of the wooden trunk-like IED. Subplots (c) and (d) correspond to the same SVD filtering: in Fig. 12 (c), where the laser rangefinder information is considered, the top side of the wooden trunk-like IED cannot be distinguished. However, if the radar height is used (Fig. 12 (d)) the reflection happening at the top side of the buried target is clearly visible.

Concerning the use of height information from GNSS-RTK, it yielded worse detection results (as it provides the height over the geoid, thus not taking into account the local variations of the soil surface), so they have not been included in the comparison.

The improvements achieved when applying the proposed correction techniques (SVD filtering based on range, and spatial alignment) can be observed when comparing Fig. 10 and Fig. 11. In the former figure, the three highest singular values are removed, whereas the latter figure corresponds to the SVD filtering presented in Section 3.3 and the co-registration technique explained in Section 3.2. In this case, the SVD filtering considers a distance threshold of 137.5 cm, i.e., C137.5, which means that those eigenimages whose maximum is located closer than 137.5 cm are removed. The application of the SVD filtering based on distance improves the detection of targets and it is especially noticed when laser rangefinder information is considered. For example, in Fig. 10 (top row) the second group of metallic plates (iii) and the VS-1.6 anti-tank landmine (x) are not detected, whereas both targets can be distinguished in Fig. 11. This improvement is also noticed in the vertical XZ cuts of the GPR-SAR images. These XZ cuts are centered at the position of the wooden trunk-like IED (Fig. 12) and at the position of the VS-1.6 anti-tank landmine (Fig. 13). In the case of the anti-tank landmine, it can be observed that the reflection detected is the one happening at the bottom part of the landmine. The reason why this reflection is detected and not the one occurring on top of the landmine is because the latter is closer to the surface, so it is partially masked by the reflection happening at the air-soil interface.

In order to better show the effect of the co-registration, in Fig. 14 the

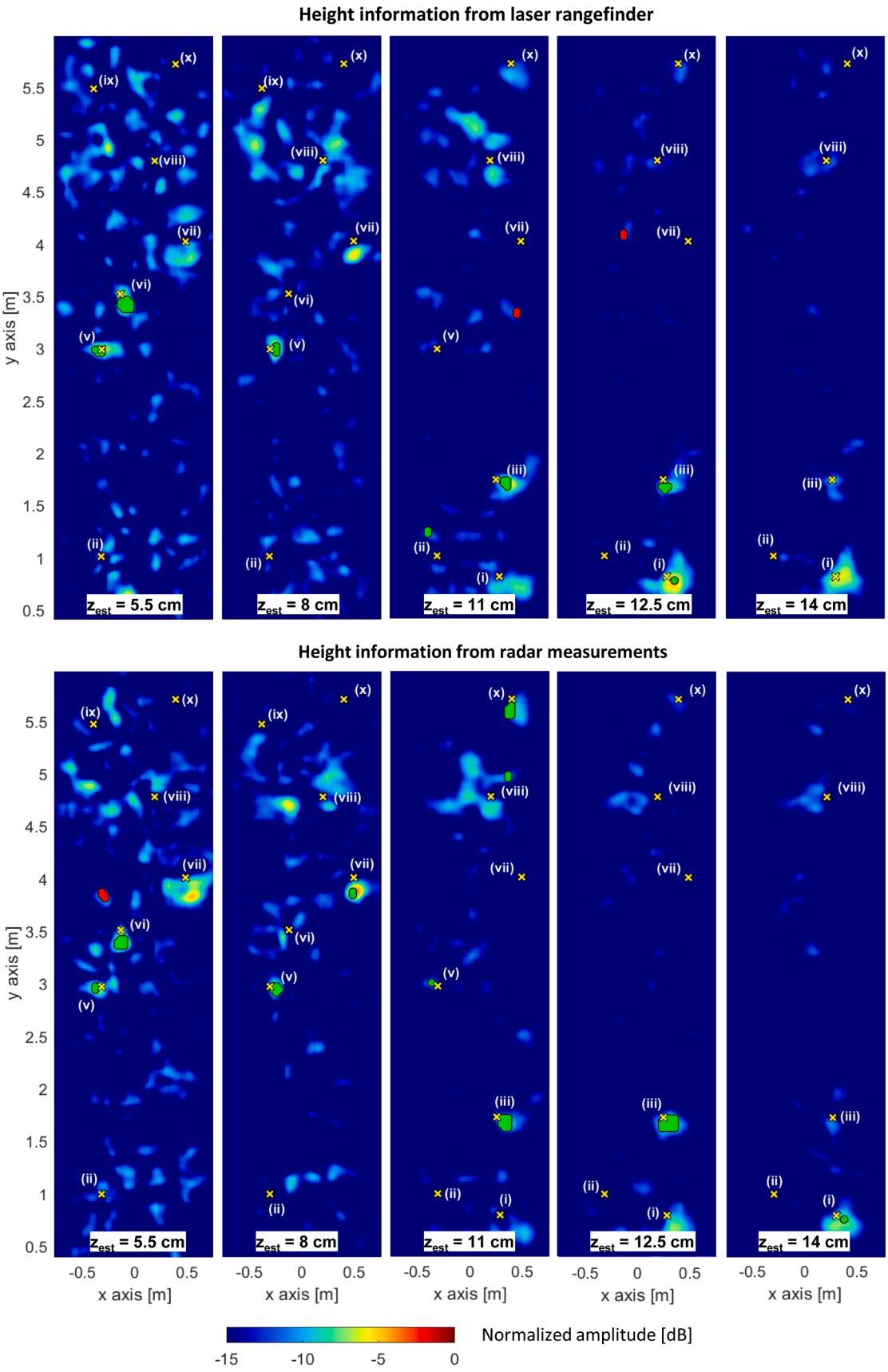

Fig. 11. Detection results in the first validation scenario when using height information from the laser rangefinder (upper row) and from the radar measurements (lower row). SVD filtering applied: removal of eigenimages whose maximum is located closer than C137.5. Co-registration is also applied.

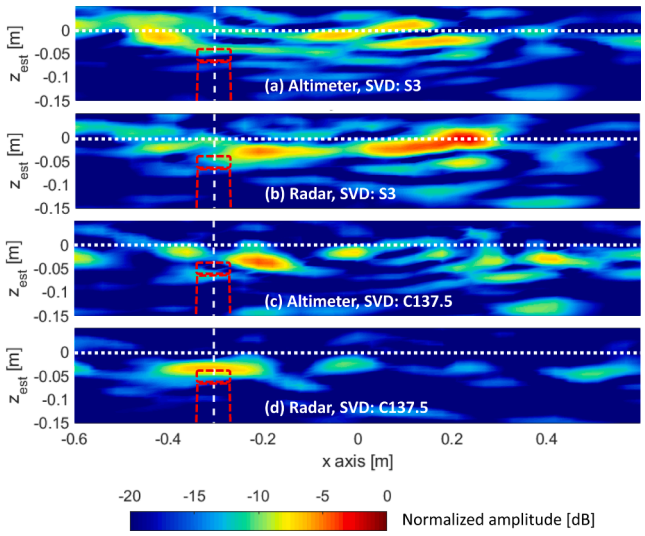

Fig. 12. Detection results in the first validation scenario. GPR-SAR images corresponding to the y = 1 m cut that intersects the position of the wooden trunk-like IED. Comparison of laser rangefinder (a,c) and radar module (b,d) height information, and SVD filtering when the three first singular values are removed (a,b) and when the eigenimages whose maximum is located closer than C137.5 are removed (c,d). White dotted line indicates the position z = 0 m. Red dashed line outlines the profile of the wooden trunk-like IED.

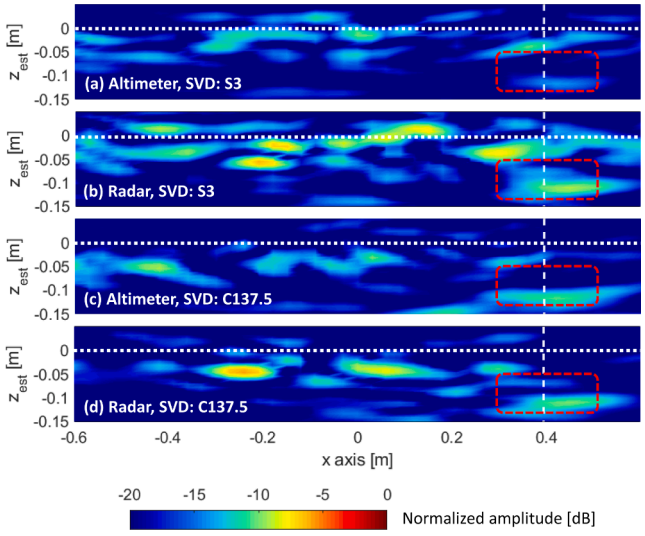

Fig. 13. Detection results in the first validation scenario. GPR-SAR images corresponding to the y = 5.7 m cut that intersects the position of the VS-1.6 anti-tank landmine. Comparison of laser rangefinder (a,c) and radar module (b,d) height information, and SVD filtering when the three first singular values are removed (a,b) and when the eigenimages whose maximum is located closer than C137.5 are removed (c,d). White dotted line indicates z = 0 m. Red dashed line outlines the profile of the VS-1.6 anti-tank landmine.

horizontal cuts of the GPR-SAR image containing the third group of metallic plates (v) and the metallic disk (vii) are compared before and after applying the co-registration. In addition, for both cases the GPR-SAR images obtained when using the height information provided by the laser rangefinder and the height estimated from the radar are presented. It can be concluded that applying the co-registration (Fig. 14 (b) and Fig. 14 (d)) improves not only the focusing of the GPR-SAR image, but also reduces the clutter level.

A quantitative analysis of the detection capability achieved in the cases depicted in Fig. 10 and Fig. 11 is conducted by counting the targets

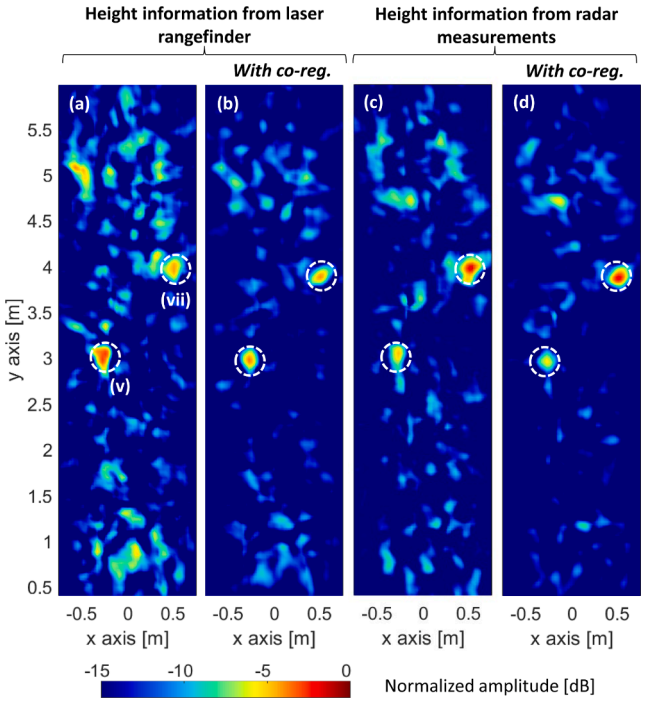

Fig. 14. Detection results in the first validation scenario when using height information from the laser rangefinder without (a) and with co-registration (b); and when using height information from the radar measurements without (c) and with co-registration (d). SVD filtering applied: removal of eigenimages whose maximum is located closer than C137.5.

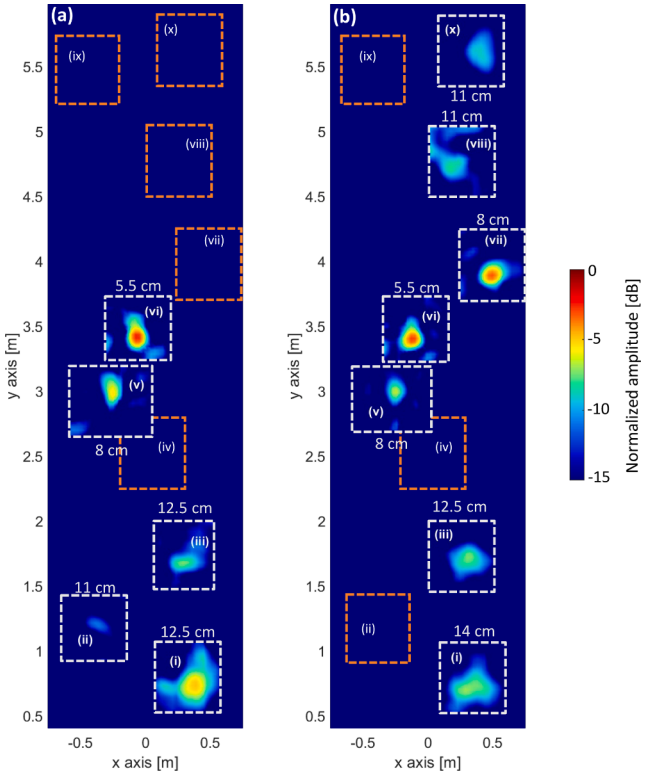

Fig. 15. Composition of the detection results based on the CFAR detections in the first validation scenario when using (a) height information from the laser rangefinder, and (b) from the radar measurements. Distance-based SVD filtering and co-registration are applied in both cases. Orange areas indicate zones where targets were buried, but not automatically detected by the CFAR algorithm.

Fig. 16. Picture of the UAV prototype while scanning the second validation scenario.

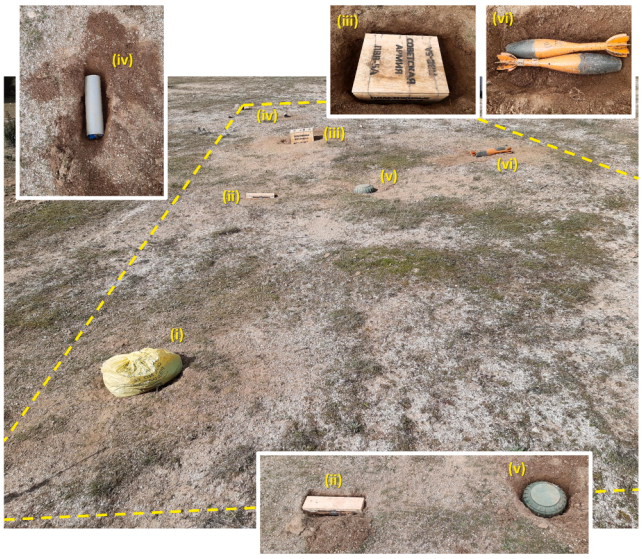

Fig. 17. Picture of the targets buried in the second validation scenario. (i) Plastic bag filled with paper, (ii) wooden pressure plate, (iii) wooden box filled with plasterboard, (iv) plastic PVC pipe, (v) VS-1.6 anti-tank plastic landmine (VS-1.6, 2021), and (vi) metallic mortar shells.

Table 3
Second validation scenario. Buried targets.

Object	Size (cm)	Depth (cm)	Other specs.
(i) Plastic bag filled with paper	30ø aprox.	5	
(ii) Wooden pressure plate	25 long × 7 wide	4	
(iii) Wooden box filled with plasterboard	30 long × 25 wide × 20 thick	5	
(iv) Plastic PVC pipe	8ø × 20 long	5	
(v) VS-1.6 anti-tank landmine (VS-1.6, 2021)	22ø × 9.2 thick	4	No metal content
(vi) Two 81 mm mortar shells	39 long × 8.1ø	8	Metallic targets

found by the CFAR detector. Detection results are summarized in Table 2, where the depth at which the CFAR detector found the targets is indicated, concluding that the best detection capabilities were obtained considering the height estimated from radar measurements and using the proposed improved processing techniques (distance-based SVD filtering and co-registration). In addition, in order to facilitate the comparison of the results, two images have been created based on the CFAR results obtained when considering the height provided by the laser rangefinder and when using the one estimated from radar measurements (applying in both cases distance-based SVD filtering and co-registration). These images, shown in Fig. 15, are composed extracting the area of the GPR-SAR image around the position where a target has been detected by the CFAR algorithm. The comparison of these images also supports the conclusion that the height estimated by the radar provides, in general, better results.

4.2. Second validation scenario

The second validation scenario is located at the Spanish military training and shooting range "El Palancar", located north of Madrid (SAFEDRONE, 2021). First, the relative permittivity of the soil was estimated (Alvarez et al., 2017), finding it to be around $\varepsilon_r = 4$. It must be pointed out that the soil of this scenario is significantly drier than in the first one (airfield of the University of Oviedo).

The scanned area, shown in Fig. 16 and Fig. 17, has a size of 12 m along-track and 4.5 m across-track, i.e., 6 times larger than the first validation example. As in the first validation case, the spacing between consecutive along-track sweeps was 5 cm and the flight height was set to 1.5 m above ground. A video of the UAV performing the scan on this second validation scenario can be watched in the provided multimedia file entitled "videoExample2.mp4".

Experts in counter IED techniques were in charge of burying the IEDs and landmines as close as possible to realistic scenarios, also including some fake targets to assess the detection capabilities of the airborne-based GPR system. These targets are listed in Table 3 and a picture is shown in Fig. 17.

Horizontal cuts of the GPR-SAR image are shown in Fig. 18, where results considering the laser rangefinder information (Fig. 18 (a.1) - Fig. 18 (a.3)) and the height extracted from radar measurements (Fig. 18 (b.1) - Fig. 18 (b.3)) are compared. CFAR detector is applied to the cuts of the GPR-SAR image. The true position of the targets is denoted with a yellow 'x' except for the larger ones, i.e. the plastic bag filled with paper (i), the wooden box (iii), and the two 81 mm mortar shells (vi). In these cases, the position is outlined with a yellow circle, rectangle, and ellipse, respectively.

When the laser rangefinder height is considered (Fig. 18 (a)), the plastic bag filled with paper (i), the wooden box (iii), and VS-1.6 anti-tank landmine are identified with the CFAR detector. The two 81 mm mortar shells can be fairly detected in the GPR-SAR image (Fig. 18 (a.2) and (a.3)). In contrast, when the height information is estimated from radar measurements (Fig. 18 (b)), the CFAR detector finds not only the two 81 mm mortar shells (vi) but also the plastic PVC pipe (iv).

The improvement on the image quality achieved with the proposed processing methods can be observed comparing Fig. 18 (b) (SVD filtering removing the three highest singular values and without co-registration) and Fig. 18 (c) (distance-based SVD filtering with C137.5 and co-registration). Both sets of images were obtained using the height estimated from the radar measurements. As it can be seen, the image obtained with the proposed improvements is less cluttered, which enables better detection capabilities. In particular, when the improvements are applied, the CFAR detector is able to detect the six buried targets. It should also be noted that some of the non-metallic buried targets have a thickness larger than the range resolution of the radar system, so the reflections happening at both the upper and lower soil-target interfaces are detected. For example, the reflection happening at the bottom of the anti-tank landmine (v) is observed at $z_{est} = 12$ cm in the three analyzed cases shown in Fig. 18.

In this scenario, the improvement in the detection thanks to co-registration is also noticeable, specially in the case of small targets. To illustrate this, Fig. 19 shows the GPR-SAR image centered at the position of the wooden pressure plate before (a) and after (b) applying co-registration. Not only the dynamic range of the target is improved, but also a better estimation of the shape of this target is obtained.

In a similar fashion to scenario 1, a composition of the detection results based on the CFAR detections is shown in Fig. 20 when

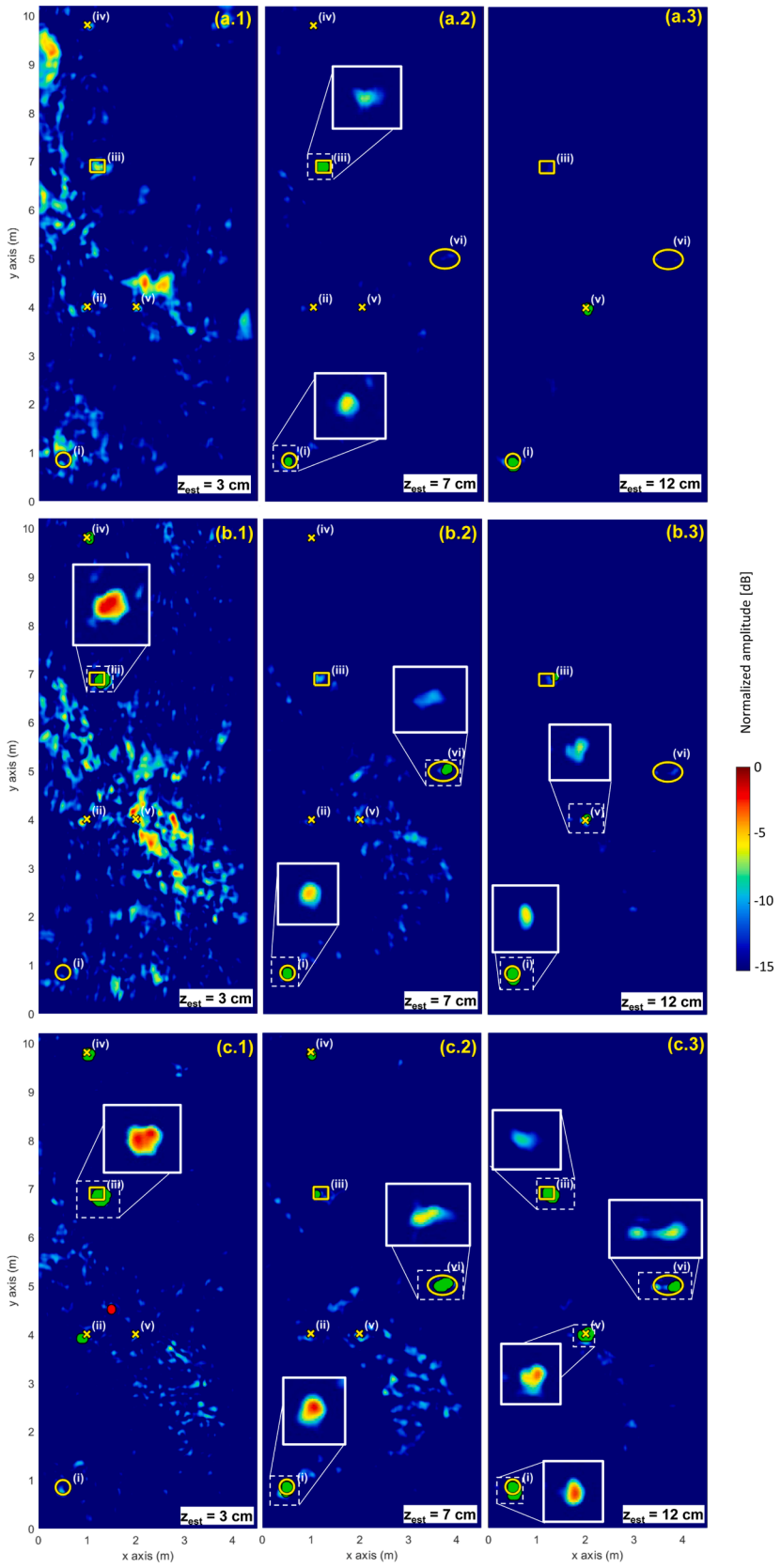

Fig. 18. Detection results in the second validation scenario. Horizontal cuts for $z_{est} = 3$ cm, $z_{est} = 7$ cm, and $z_{est} = 12$ cm. (a) Using height information from laser rangefinder and SVD filtering based on removing the highest three singular values. (b) Using height information from radar measurements and SVD filtering based on removing the highest three singular values. (c) Using height information from radar measurements and distance-based SVD filtering with C137.5 and co-registration.

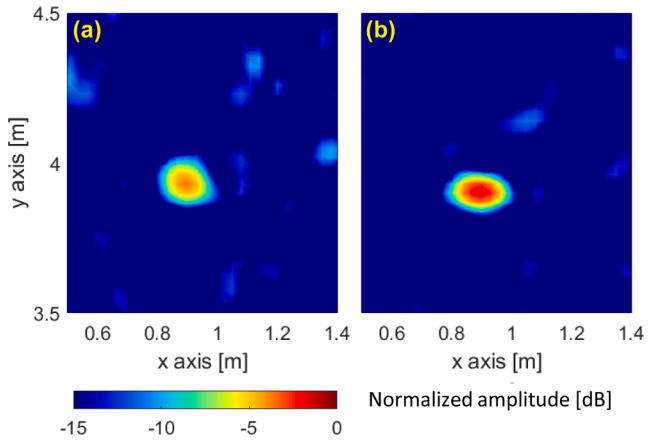

Fig. 19. GPR-SAR image centered at the position where the wooden pressure plate (ii) is located with $z_{est} = 2$ cm. Height information from radar measurements and distance-based SVD filtering with C137.5. (a) Without co-registration. (b) With co-registration.

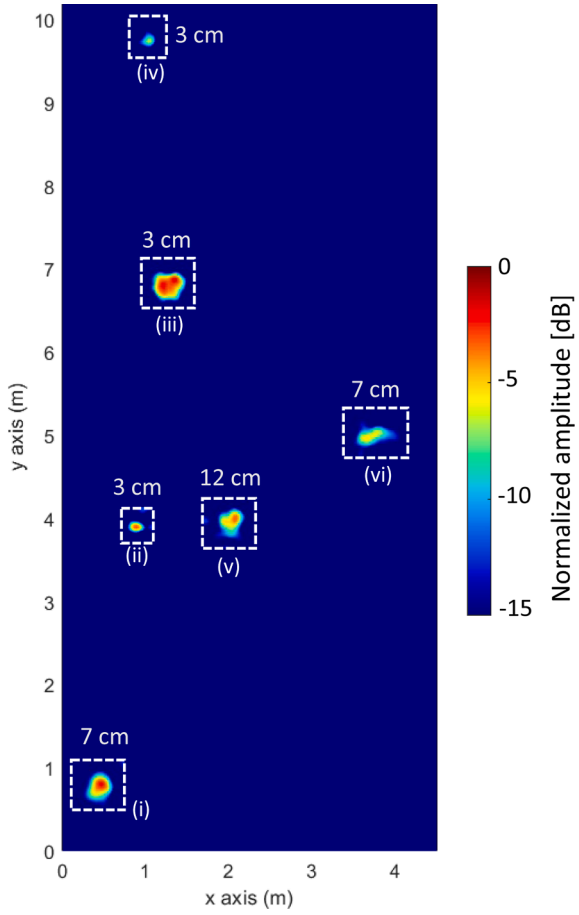

Fig. 20. Composition of the detection results based on the CFAR detections in the second validation scenario. The height was estimated from the radar measurements, and distance-based SVD filtering and co-registration are applied.

considering all the improvements proposed in this contribution. In this case, all targets have been detected both by inspecting the GPR-SAR images and by the CFAR algorithm.

Finally, the detection results for the second scenario achieved with the techniques described in this contribution are compared in Table 4.

Table 4
Targets detected in scenario 2.

Method			Target					
Height	SVD	Coreg.	(i)	(ii)	(iii)	(iv)	(v)	(vi)
Laser	S1	–	3		1			
	S2	–	3		3		1	1
	S3	–	3		3		2	1
	C135	–	3		3	1	3	3
	C137.5	–	3		3	1	3	3
	C135	Yes	3	1	3	2	3	
	C137.5	Yes	3	1	3	2	3	3
Radar	S1	–	2		3			
	S2	–	3		3	2	2	2
	S3	–	3		3	2	3	2
	C135	–	3		3	3	3	3
	C137.5	–	3	1	3	2	3	3
	C135	Yes	3	2	3	3	3	3
	C137.5	Yes	3	2	3	3	3	3

Laser: height information from laser rangefinder.
Radar: height information from radar measurements.
SVD SX: SVD filtering removing the X highest singular values
SVD CX: distance-based SVD filtering;
X is the threshold distance (in cm).
Coreg.: co-registration method is applied.

Detection key:
Empty = target not detected.
1 = poor detection (0–5 dB above clutter, no CFAR detection, e.g. Fig. 18 (a.2), target (vi)).
2 = fair detection (0–5 dB above clutter, CFAR detection, e.g. Fig. 18 (a.3), target (v)).
3 = clear detection (> 5 dB above clutter, CFAR detection, e.g. Fig. 18 (a.2), target (iii)).

These results are assigned a score according to the following criteria: 1 corresponds to poor detection (qualitative detection ⩽5 dB above clutter, without CFAR detection), 2 to fair detection (qualitative detection ⩽5 dB above clutter, and CFAR detection) and 3 to clear detection (qualitative detection >5 dB above clutter, and CFAR detection). Two of the largest targets, the plastic bag filled with papers (i) and the wooden box (iii), are detected in all cases. However, small targets such as the wooden pressure plate (ii) and the plastic PVC pipe (iv) are detected only when considering height information from radar measurements, distance-based SVD filtering, and/or co-registration. In the case of distance-based SVD filtering, thresholds of C135 and C137.5 were assessed, finding that the latter provided the best detection results.

5. Conclusions

This contribution has analyzed several issues that affect GPR-SAR images obtained with airborne-based GPR systems (Gonzalez et al., 2017; Garcia-Fernandez et al., 2020), proposing methodologies to mitigate or correct them. It has been shown that better GPR-SAR images are retrieved when the height information extracted from the GPR measurements is considered (instead of the height provided by the laser rangefinder). It was also found that due to slightly different UAV tilting (i.e., radar look angle) when conducting along-track sweeps in forward and backward directions, a small shifting happens between the GPR-SAR images obtained when considering the forward or the backward sweeps. A technique named co-registration has been introduced to correct it and provide a better focused GPR-SAR image. Finally, a distance-based SVD filtering technique has also been proposed in order to improve air-ground clutter suppression.

The performance achieved with the airborne-based GPR system (Garcia-Fernandez et al., 2020) together with the improvements presented in this contribution can been compared with the results obtained by other airborne-based GPR architectures. First, it must be pointed out that several airborne-based GPR systems do not apply SAR processing (e.g. (Colorado et al., 2017; Sipos and Gleich, 2020)), thus limiting the

resolution and the detection capabilities. Apart from the DL-GPR prototype used in this contribution (Garcia-Fernandez et al., 2020), only the airborne side-looking GPR presented in Schartel et al. (2020) uses SAR processing and it is also capable to provide 3D GPR-SAR images. The scanned area is also similar (32.8 m^2 in Schartel et al. (2020), and 46 m^2 in the second validation scenario of the present contribution).

Although the systems architecture is different (this contribution is a DLGPR architecture, whereas (Schartel et al., 2020) is a side-looking GPR), both airborne-based GPR systems are able to detect the same kind of threats, such as pressure plates and anti-tank landmines. In any case, it must be pointed out that a controlled scenario filled with sand was used in Schartel et al. (2020), which is a less challenging scenario than the two ones presented in this contribution (especially the first one).

Concerning the use of radar measurements to extract height information, results presented in this contribution are in line with those ones described in Burr et al. (2021), where images provided by the UAV-based side-looking GPR are improved when the ground profile is extracted from radar measurements. Compared to Burr et al. (2021), this contribution has the advantage of not requiring two non-contiguous frequency bands, thus simplifying the hardware complexity (as the GPR radar itself is used to estimate the height). Nevertheless, for other UAV-based remote sensing applications, the choice of the appropriate sensor or method to obtain the height above the ground is eventually a trade-off that takes into account the scenario, the operative height, and even the UAV platform dynamics.

Funding

This work has been funded by the Ministry of Defence - Government of Spain and by the University of Oviedo under Contract 2019/SP03390102/00000204/ CN-19-002 (“SAFEDRONE”); by the Ministerio de Ciencia, Innovación y Universidades of Spain/FEDER under project RTI2018-095825-B-I00 (“Millihand”) and project PID2021-122697OB-I00; by the Ministry of Universities of Spain and European Union - NextGenerationEU - under grants MU-21-UP2021-030-53519863 and MU-21-UP2021-030-71667225; and by Gobierno del Principado de Asturias/FEDER under grant AYUD/2021/51706.

Declaration of Competing Interest

The authors declare that they have no known competing financial interests or personal relationships that could have appeared to influence the work reported in this paper.

Acknowledgment

The authors would like to acknowledge Col. José Luis Mingote Abad and Cap. Santiago García Ramos for their advice concerning the placement of the IEDs and landmines, for the preparation of the second validation scenario located at the Spanish military training and shooting range “El Palancar”, as well as for the supervision of the “SAFEDRONE” project. The authors would also like to thank the personnel of the Counter Improvised Explosive Devices Center of Excellence (C-IED CoE) (C-IED CoE, 2021) and the Ministry of Defense of Spain involved in the preparation of the second validation scenario.

The technology presented in this contribution is protected by the patents listed in Gonzalez et al. (2017).

Appendix A. Supplementary material

Supplementary data associated with this article can be found, in the online version, at https://doi.org/10.1016/j.isprsjprs.2022.04.014.

References

Abujarad, F., Nadim, G., Omar, A., 2018. Clutter reduction and detection of landmine objects in ground penetrating radar data using singular value decomposition (SVD). In: Proc. of the 2018 11th German Microwave Conference (GeMiC), pp. 1–4.

Alvarez, Y., Garcia, M., Arboleya, A., Gonzalez, B., Vaqueiro, Y.R., Las-Heras, F., Pino, A. G., 2017. SAR-based technique for soil permittivity estimation. Int. J. Remote Sens. 38, 5168–5186.

Bestagini, P., Lombardi, F., Lualdi, M., Picetti, F., Tubaro, S., 2021. Landmine detection using autoencoders on multipolarization gpr volumetric data. IEEE Trans. Geosci. Remote Sens. 59, 2035–2039.

Bi, W., Zhao, Y., An, C., Hu, S., 2018. Clutter Elimination and Random-Noise Denoising of GPR Signals Using an SVD Method Based on the Hankel Matrix in the Local Frequency Domain. Sensors 18, 1–15.

Burr, R., Schartel, M., Grathwohl, A., Mayer, W., Walter, T., Waldschmidt, C., 2021. UAV-borne FMCW InSAR for focusing buried objects. IEEE Geosci. Remote Sens. Lett. 1–5. https://doi.org/10.1109/LGRS.2021.3094165.

Counter improvised explosive devices center of excellence (C-IED CoE), 5 2021. https://www.ciedcoe.org/.

Clark, W., Burns, B., Sherbondy, K., Ralston, J., Rappaport, C., 2005. Surface effects on ground penetrating radar imagery. In: Proc. of the 2005 IEEE Antennas and Propagation Society International Symposium, pp. 404–407.

Colomina, I., Molina, P., 2014. Unmanned aerial systems for photogrammetry and remote sensing: A review. ISPRS J. Photogramm. Remote Sens. 92, 79–97. https://doi.org/10.1016/j.isprsjprs.2014.02.013. URL https://www.sciencedirect.com/science/article/pii/S0924271614000501.

Colorado, J., Perez, M., Mondragon, I., Mendez, D., Parra, C., Devia, C., Martinez-Moritz, J., Neira, L., 2017. An integrated aerial system for landmine detection: SDR-based ground penetrating radar onboard an autonomous drone. Adv. Robot. 31, 791–808.

Comite, D., Ahmad, F., Dogaru, T., Amin, M.G., 2018. Adaptive detection of low-signature targets in forward-looking gpr imagery. IEEE Geosci. Remote Sens. Lett. 15, 1520–1524.

Comite, D., Ahmad, F., Amin, M.G., Dogaru, T., 2021. Forward-looking ground-penetrating radar: Subsurface target imaging and detection: A review. IEEE Geosci. Remote Sens. Mag. Early Access. https://doi.org/10.1109/MGRS.2020.3048368.

Daniels, D.J., 2006. A review of GPR for landmine detection. Sens. Imaging Int. J. 7, 90–123. https://doi.org/10.1007/s11220-006-0024-5.

Garcia-Fernandez, M., Alvarez-Lopez, Y., Rodriguez-Vaqueiro, Y., Gonzalez-Valdes, B., Arboleya-Arboleya, A., Las-Heras, F., Pino-Garcia, A., 2017. SVD-based clutter removal technique for GPR. IEEE AP-S Symposium on Antennas and Propagation 2017, 2369–2370.

Garcia-Fernandez, M., Alvarez-Lopez, Y., Heras, F.L., 2019. Autonomous Airborne 3D SAR Imaging System for Subsurface Sensing: UWB-GPR on board a UAV for Landmine and IED Detection. Remote Sens. 11, 2357. https://doi.org/10.3390/rs11202357.

Garcia-Fernandez, M., Alvarez-Lopez, Y., Las-Heras, F., 2020. Airborne multi-channel ground penetrating radar for improvised explosive devices and landmine detection. IEEE Access 8, 165927–165943.

Gauthier, Y., Bernier, M., Fortin, J.-P., 1998. Aspect and incidence angle sensitivity in ERS-1 SAR data. Int. J. Remote Sens. 19 (10), 2001–2006. https://doi.org/10.1080/014311698215117.

GNSS-RTK from Topcon, 5 2020. https://www.topconpositioning.com/oem-components-technology/.

Gonzalez-Diaz, M., Garcia-Fernandez, M., Alvarez-Lopez, Y., Las-Heras, F., 2020. Improvement of GPR SAR-based techniques for accurate detection and imaging of buried objects. IEEE Trans. Instrument. Meas. 6, 3126–3138.

Gonzalez, P., Garcia, E., Estremera, J., Armada, M.A., 2005. DYLEMA: using walking robots for landmine detection and location. Int. J. Syst. Sci. 36, 545–558.

Gonzalez, B., Alvarez, Y., Arboleya, A., Vaqueiro, Y.R., Garcia, M., Las-Heras, F., Pino, A. G., 2017. Airborne systems and detection methods localization and production of images of buried objects and characterization of the composition of the subsurface, patents ES2577403B2, EP3407007B1, CN109073348B, US10895636B2 (7 2017). https://patents.google.com/patent/WO2017125627A1/en.

Hasan, S., Montzka, C., Rüdiger, C., Ali, M., Bogena, H.R., Vereecken, H., 2014. Soil moisture retrieval from airborne l-band passive microwave using high resolution multispectral data. ISPRS J. Photogramm. Remote Sens. 91, 59–71. https://doi.org/10.1016/j.isprsjprs.2014.02.005. URL https://www.sciencedirect.com/science/article/pii/S0924271614000422.

Hügler, C., Roos, F., Schartel, M., Geiger, M., Waldschmidt, C., 2018. Radar taking off. IEEE Microwave Mag. 19, 43–53.

Ismail, A., Elmogy, M., ElBakry, H., 2014. Landmines detection using autonomous robots: A survey. Int. J. Emerg. Trends Technol. Comput. Sci. 3, 183–187.

Johansson, E.M., Mast, J.E., 1994. Three-dimensional ground-penetrating radar imaging using synthetic aperture time-domain focusing. In: Udpa, S.S., Han, H.C. (Eds.), Advanced Microwave and Millimeter-Wave Detectors, vol. 2275. International Society for Optics and Photonics, SPIE, pp. 205–214. https://doi.org/10.1117/12.186717.

Jol, H.M., 2009. Ground Penetrating Radar: Theory and Applications. Elsevier, Amsterdam.
Klein, K., Uysal, F., Cuenca, M., Otten, M., de Wit, J., 2020. IED command wire detection using multi-aspect processing on SAR images. In: Proceedings of the 2020 IEEE Radar Conference (RadarConf20), pp. 1–6.
Lambot, S., Slob, E.C., Bosch, I.V.S., Stockbroeckx, B., Scheers, B., Vanclooster, M., 2004. Estimating soil electric properties from monostatic ground penetrating radar signal inversion in the frequency domain. Water Resour. Res. 40, 1–12.
Lee, J.S., Nguyen, C., Scullion, T., 2004. A novel, compact, low-cost, impulse ground-penetrating radar for nondestructive evaluation of pavements. IEEE Trans. Instrum. Meas. 53, 1502–1509. https://doi.org/10.1109/TIM.2004.827308.
Leuschen, C.J., Plumb, R.G., 2001. A matched-filter-based reverse-time migration algorithm for ground-penetrating radar data. IEEE Trans. Geosci. Remote Sens. 39, 929–936. https://doi.org/10.1109/36.921410.
LIDAR altimeter from Lightware Optoelectronics, 5 2020. https://lightwarelidar.com/collections/lidar-rangefinders/products/sf11-b-50-m.
Llossera, M.V., Cardona, M., Blanch, S., Camps, A., Monerris, A., Corbella, I., Torres, F., Duff, N., 2005. L-band dielectric properties of different soil types collected during the MOUSE 2004 field experiment. In: Proceedings of the 2005 IEEE International Geoscience and Remote Sensing (IGARSS), pp. 1109–1112.
Lopera, O., Slob, E.C., Milisavljevic, N., Lambot, S., 2007. Filtering Soil Surface and Antenna Effects From GPR Data to Enhance Landmine Detection. IEEE Trans. Geosci. Remote Sens. 45, 707–717.
Ludeno, G., Catapano, I., Renga, A., Vetrella, A.R., Fasano, G., Soldovieri, F., 2018. Assessment of a micro-uav system for microwave tomography radar imaging. Remote Sens. Environ. 212, 90–102. https://doi.org/10.1016/j.rse.2018.04.040.
m:explore UWB radar from ILMSens, 5 2021. https://www.ilmsens.com/products/m-explore/.
Makki, I., Younes, R., Francis, C., Bianchi, T., Zucchetti, M., 2017. A survey of landmine detection using hyperspectral imaging. ISPRS J. Photogramm. Remote Sens. 124, 40–53. https://doi.org/10.1016/j.isprsjprs.2016.12.009. URL https://www.sciencedirect.com/science/article/pii/S0924271616306451.
Martinez-Lorenzo, J.A., Rappaport, C.M., Quivira, F., 2011. Physical limitations on detecting tunnels using underground-focusing spotlight synthetic aperture radar. IEEE Trans. Geosci. Remote Sens. 49, 65–70. https://doi.org/10.1109/TGRS.2010.2051952.
Mattes, D., Haynor, D., Vesselle, H., Lewellen, T., Eubank, W., 2001. Non-rigid multimodality image registration. Medical Imaging 2001: Image Processing 1609–1620.
Minekafon project, 5 2021. http://minekafon.org/.
Neusch, T., Sties, M., 1999. Application of the Dubois-model using experimental synthetic aperture radar data for the determination of soil moisture and surface roughness. ISPRS J. Photogramm. Remote Sens. 54 (4), 273–278. https://doi.org/10.1016/S0924-2716(99)00019-2. URL https://www.sciencedirect.com/science/article/pii/S0924271699000192.
Noviello, C., Esposito, G., Catapano, I., Soldovieri, F., 2021. Multilines imaging approach for mini-UAV radar imaging system. IEEE Geosci. Remote Sens. Lett. 1, 1–5.
Peichl, M., Schreiber, E., Heinzel, A., Kempf, T., 2014. TIRAMI-SAR - a synthetic aperture radar approach for efficient detection of landmines and uxo. In: EUSAR 2014 – 10th European Conference on Synthetic Aperture Radar, pp. 1–4.
Plotnick, D.S., Marston, T.M., 2018. Utilization of aspect angle information in synthetic aperture images. IEEE Trans. Geosci. Remote Sens. 56 (9), 5424–5432. https://doi.org/10.1109/TGRS.2018.2816462.
Rappaport, C.M., 2006. Radar-based altitude over ground estimation of UAVs. In: Proc. of the 2006 IEEE MTT-S International Microwave Symposium Digest, pp. 280–283.
Rosen, E.M., Ayers, E., 2005. Assessment of down-looking GPR sensors for landmine detection. In: Harmon, R.S., Broach, J.T., J.H.H. Jr. (Eds.), Detection and Remediation Technologies for Mines and Minelike Targets X, vol. 5794. International Society for Optics and Photonics, SPIE, pp. 423–434. https://doi.org/10.1117/12.603831.
Roussi, C., Xique, I., Burns, J., Hart, B., 2019. Buried object imaging using a small UAS-based GPR. In: Proceedings of the SPIE 11012, Detection and Sensing of Mines, Explosive Objects, and Obscured Targets XXIV, vol. 11012, pp. 1–9. https://doi.org/10.1117/12.2518997.
SAFEDRONE project - intermediate validation trials. C-IED CoE newsletter, July 2021. page 13 of 24., 7 2021. https://www.ciedcoe.org/index.php/docman/newsletter-cied-coe/850-newsletter-20july-202021/file.
Sato, M., Feng, X., Fujiwara, J., 2005. Handheld GPR and MD sensor for landmine detection. In: IEEE Antennas and Propagation Society International Symposium, pp. 1–4.
Schartel, M., Burr, R., Schoeder, P., Rossi, G., Hügler, P., Mayer, W., Waldschmidt, C., 2018. Radar-based altitude over ground estimation of UAVs. In: Proc. of the 3rd International Workshop on Advanced Ground Penetrating Radar (IWAGPR), pp. 103–106.
Schartel, M., Burry, R., Bahnemannz, R., Mayer, W., Waldschmidt, C., 2020. An experimental study on airborne landmine detection using a circular synthetic aperture radar. https://arxiv.org/abs/2005.02600.
Schreiber, E., Heinzel, A., Peichl, M., Engel, M., Wiesbeck, W., 2019. Advanced buried object detection by multichannel, UAV/drone carried synthetic aperture radar. In: Proceedings of the 2019 13th European Conference on Antennas and Propagation (EuCAP), pp. 1–5.
Sipos, D., Gleich, D., 2020. A lightweigth and low-power UAV-borne ground penetrating radar design for landmine detection. Sensors 20, 2234.
S.M.M. et al., 2008. Detection and location of partial discharges in power transformers using acoustic and electromagnetic signals. IEEE Trans. on Dielectrics Electr. Insulat. 15, 1576–1583.
Solimene, R., Cuccaro, A., Dell'Aversano, A., Catapano, I., Soldovieri, F., 2014. Ground Clutter Removal in GPR Surveys. IEEE J. Sel. Top. Appl. Earth Observ. Remote Sens. 7, 792–798.
Spreading wings s1000+ from DJI, 5 2021. https://www.dji.com/spreading-wings-s1000-plus.
Styner, M., Brechbühler, C., Székely, G., Gerig, G., 2000. Parametric estimate of intensity inhomogeneities appliedo to MRI. IEEE Trans. Med. Imaging 19, 153–165.
Taylorl, J.D., 2019. Advanced Ultrawideband Radar: Signals, Targets, and Applications. CRC Press, Tayor and Francis Group, Boca Raton, USA.
TS-50 anti-personnel landmine, 5 2021. https://en.wikipedia.org/wiki/TS-50_mine.
TSA600 vivaldi antenna from RFSpace, 5 2021. http://rfspace.com/RFSPACE/Antennas_files/TSA600.pdf.
van der Merwe, A., Gupta, I.J., 2000. A Novel Signal Processing Technique for Clutter Reduction in GPR Measurements of Small, Shallow Land Mines. IEEE Trans. Geosci. Remote Sens. 38, 2627–2637.
VS-1.6 anti-tank landmine, 5 2021. https://en.wikipedia.org/wiki/VS-1.6_mine.
Won, I.J., Keiswetter, D.A., Bell, T.H., 2001. Electromagnetic induction spectroscopy for clearing landmines. IEEE Trans. Geosci. Remote Sens. 39 (4), 703–709.
Yoo, L.-S., Lee, J.-H., Ko, S.-H., Jung, S.-K., Lee, S.-H., Lee, Y.-K., 2020. A drone fitted with a magnetometer detects landmines. IEEE Geosci. Remote Sens. Lett. 17, 182–195.